L Vignitchouk et al.

Beryllium droplet cooling and distribution in the ITER vessel after a disruption

Beryllium droplet cooling and distribution in the ITER vessel after a disruption

L Vignitchouk[a], S Ratynskaia[a], P Tolias[a], G De Temmerman[b], M Lehnen[b] and S W Lisgo[b]

a KTH Royal Institute of Technology, Space and Plasma Physics, Stockholm, Sweden
b ITER Organization – Route de Vinon-sur-Verdon – CS 90 046 – 13067 St-Paul-lez-Durance Cedex, France

E-mail: `ladislas.vignitchouk@ee.kth.se`

Abstract. The motion and temperature evolution of beryllium droplets formed by first wall surface melting after a disruption in ITER are simulated by the MIGRAINe dust dynamics code. From the analysis of a wide range of initial conditions and disruption scenarios, the initial droplet size emerges as a parameter of crucial importance, influencing the droplets' cooling rate as well as their ability to migrate away from their injection point. The effect of the neutral gas composition in the chamber after the disruption is considered, with a focus on the potential presence of steam from loss-of-coolant accidents. While steam may chemically react with hot beryllium, constituting a risk of hydrogen explosion, it is shown to significantly enhance droplet cooling.

1. Introduction

Dust generated in the ITER nuclear phases will be activated, tritiated, chemically reactive, and toxic. For this reason, the ITER Licensing agreement requires that the quantity of dust in the vacuum vessel must remain below given limits [1]. The maximum amount of mobilizable dust in the vessel is 1000 kg. Another limit relates to the chemical reactivity of dust and the potential hydrogen production during the reaction of hot dust particles with steam, which is to be limited to 2.5 kg H_2 to prevent the risk of hydrogen explosion following the accidental ingress of air and water into the vessel. Assuming complete reaction with steam, this yields an amount of 11 kg Be on hot surfaces (or 230 kg W).

Several mechanisms may contribute to dust formation. Amongst them, the most significant are expected to be droplet ejection during transient events, especially from melting of the Be wall during disruptions, and flaking of layers forming as a result of first wall erosion, material migration and subsequent deposition [2]. Depending on the deposition conditions, these layers will contain various amounts of tritium, and can spontaneously delaminate when the layer thickness is higher than a critical value, which will be a function of the layer mechanical properties. Material ejection from molten material can be caused by several mechanisms such as the explosion of vapour bubbles inside the liquid layer, instabilities at the plasma-liquid interface (Rayleigh-Taylor, Kelvin-Helmholtz) and $\boldsymbol{j} \times \boldsymbol{B}$ forces generated in the liquid metal by eddy currents [3]. Droplet/particle ejection has been studied experimentally in disruption simulation experiments performed in plasma guns with W surfaces (e.g. [4, 5]) and more recently with Be (e.g. [6]), although the plasma pressure during those experiments is orders of magnitude higher than what is expected in ITER. In addition, particle ejection has been observed during disruptions at JET [7] while re-solidified droplets are observed on the surface of neighbouring tiles. Given the high stored energy of ITER plasmas, significant amounts of hot metallic particles might be produced during disruptions.

The aim of this paper is to study the cooling of droplets ejected from molten Be surfaces during vertical displacement events (VDE) mitigated by massive gas injection for various disruption scenarios. The MIGRAINe dust dynamics code [8, 9] is used to simulate the motion and temperature evolution of the droplets for a wide range of initial conditions including the particle size, speed and ejection angle. The results are analyzed to determine how long those droplets could remain hot enough to react with steam during an accidental ingress and to localize preferred accumulation sites of the

re-solidified particles, as well as the location of liquid splashes on the chamber wall.

2. Method

Given the highly complex and transient nature of disrupting plasmas, simplifying assumptions are required to construct plasma profiles input relevant for a wide class of disruptions. The simulations reported here are split into two stages, hereafter referred to as the plasma stage and the gas stage. The plasma stage consists in solving the full set of dust-plasma interaction equations in MIGRAINe [8, 9], with spatially uniform plasma profiles corresponding to the current quench phase of a VDE. After a time τ_{plasma}, the plasma is switched off and the vacuum vessel is assumed to be uniformly filled with neutral gas, whose composition and pressure are chosen to mimic disruption mitigation by massive gas injection.

2.1. Heat balance in the plasma stage

According to current predictions, the plasma remaining in the ITER chamber during a current quench is sufficiently hot and dense ($n_e \sim 10^{20}$ m^{-3} and $T_e \sim 5$ eV) to lead to significant charging and heating of the droplets created at the start of the disruption. Due to the high vapour pressure of Be, this implies that a significant fraction of the droplets' mass may get vaporized by the plasma, which impacts their cooling during the gas stage. The MIGRAINe model of dust-plasma interaction, described extensively in [8], is employed to compute the time evolution of the droplets' position, velocity, size, charge and temperature as they are immersed in the surrounding plasma. Among the numerous physical processes involved, the dominant sources of charging and heating are the collection of charged species from the plasma and thermionic electron emission, though the latter is typically low owing to the large work function of Be compared to its phase transition temperatures. This prevents the formation of potential wells that affect the physics of electron collection by the droplets [10]. It is furthermore assumed that there is no preferred plasma flow during the current quench, so that the ion drag is negligible and gravity is the only force acting on the droplets. A more detailed discussion on the model's applicability is given in section 3.

2.2. Heat balance in the gas stage

Once the plasma is switched off, the simulations are greatly simplified as charging mechanisms are absent and droplet cooling only stems from gray-body thermal radiation,

conductive heat transfer with the surrounding gas and vaporization. The gas density is also assumed to be low enough for friction forces to be discarded, so that the droplets are free-falling. More precisely, the heating equation becomes

$$\frac{\mathrm{d}H_\mathrm{d}}{\mathrm{d}t} = 4\pi R_\mathrm{d}^2 \left[\varepsilon_\mathrm{d}\sigma \left(T_\mathrm{w}^4 - T_\mathrm{d}^4 \right) + \sum_\mathrm{g} h_\mathrm{g} \left(T_\mathrm{g} - T_\mathrm{d} \right) + q_\mathrm{vap} \right] \tag{1}$$

where H_d, R_d and T_d are the dust enthalpy, radius and bulk temperature, respectively, σ is the Stefan-Boltzmann constant, T_w and T_g are the temperatures of the chamber wall and the neutral gas species 'g', and q_vap accounts for vaporization and quickly becomes negligible as the droplets cool down. The dependence of the dust thermal emissivity ε_d as a function of R_d and T_d is computed from Mie theory [11] using experimental data for the electrical resistivity of beryllium [12].

For the gas pressures considered here, the collisional mean free path of the gas particles is $\lambda_\mathrm{g} \gtrsim 500~\mu$m, implying that the Knudsen number of the gas flow around the droplets is $\lambda_\mathrm{g}/R_\mathrm{d} \gtrsim 1$. In this regime, the heat transfer coefficient h_g can be estimated by [13]

$$h_\mathrm{g} = \frac{1}{1 + \frac{4R_\mathrm{d}}{15\lambda_\mathrm{g}}} \frac{\gamma_\mathrm{g} + 1}{2\left(\gamma_\mathrm{g} - 1\right)} k_\mathrm{B} \Gamma_\mathrm{g}^\mathrm{th} \tag{2}$$

where k_B is Boltzmann's constant, γ_g is the heat capacity ratio of the gas, $\Gamma_\mathrm{g}^\mathrm{th} = p_\mathrm{g}/\sqrt{2\pi m_\mathrm{g} k_\mathrm{B} T_\mathrm{g}}$ is the Maxwellian particle flux on the grain surface, with p_g the gas pressure, and m_g its molecular mass. Equation (2) assumes perfect thermal accommodation of the gas particles to T_d, which is consistent with the fact that energy reflection coefficients for Ar and Ne impinging on Be are typically below 10^{-6} [14].

Another potential heat source stems from the exothermic oxidation of Be with steam $\mathrm{Be} + \mathrm{H_2O} \rightarrow \mathrm{BeO} + \mathrm{H_2} + 367$ kJ/mol [15, 16]. The associated reaction rate can be found in [17, 18, 19] as a function of T_d up to the melting point of Be. Although, to our knowledge, no experimental data exists on liquid Be oxidation, extrapolating the measurements carried out on solid Be to $T_\mathrm{d} = 2000$ K – the maximum temperature achieved by the droplets in the simulations – the heat released by chemical reactions under a pressure of 100 Pa is found to be at most 1 % of the heat exchanged by conduction between the droplets and the water vapour. This contribution can therefore be neglected in the model.

2.3. Dust-wall collisions

Determining the amount of kinetic energy lost when a dust grain impacts the chamber wall is crucial to derive the characteristics of dust migration. Dust-wall collisions in MIGRAINe are treated according to the elastic-perfectly plastic adhesive sphere-surface impacts model by Thornton and Ning [9, 20], recently validated against experimental observations of dust-surface collisions in the sheath of magnetized plasmas [21]. Taking into account energy dissipation due to adhesive forces and plastic deformation, this model quantifies the reduction of the particle velocity component normal to the surface as a function of the mechanical properties of the materials in contact, as well as the particle size and normal velocity. A major feature of this approach is the emergence of the sticking velocity v_s, which is the minimum normal velocity the particle must have to be able to rebound. In the case where the effects of adhesion and plasticity can be treated independently, the sticking velocity has a rather simple expression

$$v_s = \frac{\sqrt{3}}{2}\pi^{1/3}\sqrt{\frac{1 + 6 \times 2^{2/3}}{5}}\left(\frac{\Gamma^5}{\rho_d^3 E^{*2} R_d^5}\right)^{1/6} \tag{3}$$

where Γ is the interface energy, E^* is the reduced Young modulus of the dust-wall contact and ρ_d is the mass density of the dust material. However, for particles smaller than several tens of μm v_s is typically too high for the coupling between adhesion and plasticity to be neglected [22], resulting in a more involved scaling of v_s with mechanical properties. This is further complicated by the fact that mechanical properties depend on temperature and size [23, 24], leading to a competition between the enhanced plasticity of hotter grains and the wider elastic range of micrometre-sized particles. Such temperature and size dependences are implemented in MIGRAINe [8] and can be visualized on figure 1.

As energy dissipation upon impact is entirely imparted on the normal component of the particle velocity in the Thornton and Ning model, surface roughness on a spatial scale comparable with the particle size can significantly affect the outcome of a collision. This effect is incorporated in MIGRAINe by randomizing the surface normal at the impact point around the macroscopic surface normal [9]. The dispersion of the random normal is controlled by the roughness parameter $\sigma_r = \sigma_{surf}/d$, where σ_{surf} is the standard deviation of the surface height and $d \sim R_d$ is the characteristic scale of the asperities along the surface. Available profilometry data for fusion-grade plasma-facing components shows both σ_{surf} and d to be of the order of a few micrometres, and design specifications for ITER impose $\sigma_{surf} \leq 6.3$ μm [25], meaning that this approach
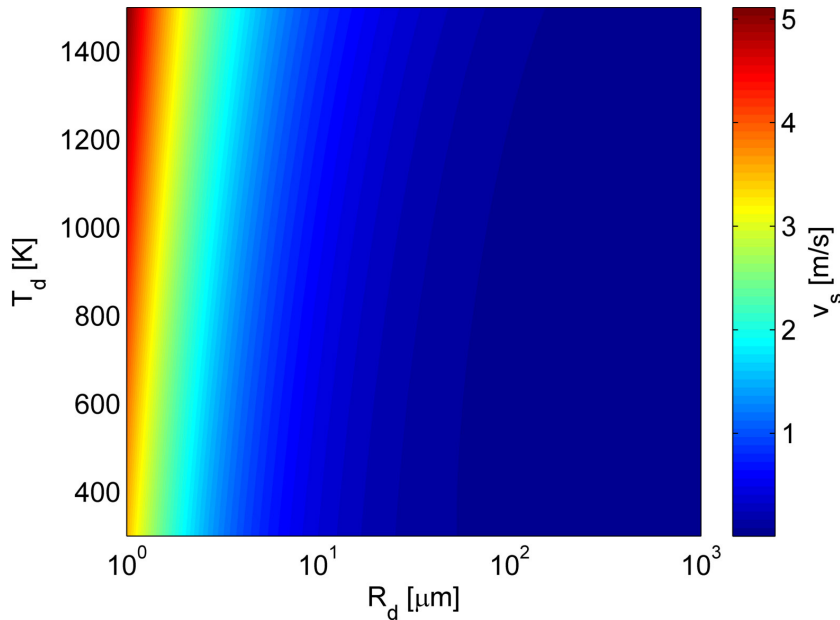
Figure 1: Sticking velocity v_{s} for the impact of a solid Be dust grain on a 350 K Be surface, as a function of the grain's radius R_{d} and temperature T_{d}.

to roughness modelling is only valid for particles smaller than approximately 10 μm. In order to qualitatively assess the effect of surface roughness for all particle sizes, the roughness parameter in MIGRAINe simulations is made to depend also on the particle size as $\sigma_{\mathrm{r}} = \min\left(1, \sigma_{\mathrm{surf}}/R_{\mathrm{d}}\right)$, with $\sigma_{\mathrm{surf}} = 6$ μm, so that particles larger than ~ 30 μm in radius are essentially unaffected by surface roughness.

2.4. Heat transfer upon contact

The cooling model described by equation (1) excludes the possibility of conductive heat transfer between the particles and the vessel wall upon contact. The necessity to quantify this cooling mechanism arises for two reasons: (i) large, solid dust particles typically have a low sticking velocity [9, 20] and require several collisions with the wall to be stopped; (ii) in the event that a particle sticks to the wall while hotter than T_{w} – particularly if it is hot enough to be chemically active – its subsequent temperature evolution is not treated by MIGRAINe.

Although the general problem of heat transfer between two metallic surfaces in contact is complex [26, 27], the main scalings and relevant timescales can be obtained by considering an idealized situation involving a hot sphere in perfect contact with a cold half-space. Assuming that the bodies in contact are made of the same material and that its thermal properties are temperature-independent, the heat equation can be
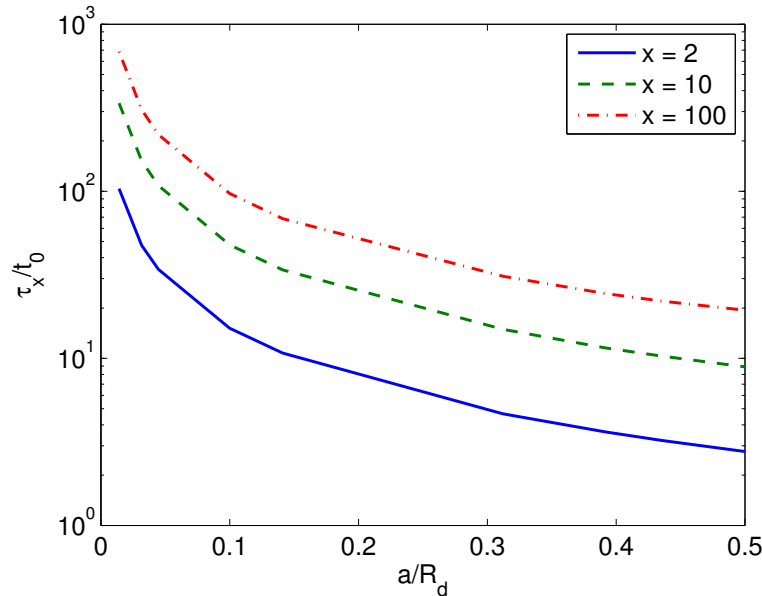
Figure 2: Normalized time τ_x required for the temperature difference between a dust grain and a wall made of the same material to be reduced by a factor x, as a function of the contact radius a. Impact speeds of a few m/s are typically expected to result in $a/R_d < 0.1$ [28].

cast in a simple non-dimensional form. Numerical solutions can then be computed from available finite-element schemes and depend only on the geometry of the domain, that is on the contact radius a between the particle and the surface. Figure 2 details the results of COMSOL Multiphysics simulations, yielding the values of the characteristic cooling times as a function of the contact radius, normalized to the heat diffusion time across the dust radius, given by $t_0 = R_d^2/D$, where D is the thermal diffusivity of the metal. In the case of different materials in contact, an effective diffusivity can be defined and t_0 remains of the same order of magnitude.

The characteristic cooling time must be compared with the duration of the dust-wall contact, for which a lower-bound estimate is obtained from the collision time according to Hertz's theory of elastic contacts [29]

$$t_{\text{Hertz}} = 5.1 R_d v^{-1/5} \left(\frac{\rho_d}{E^*}\right)^{2/5} \tag{4}$$

where v is the incident velocity of the particle. Using $\rho_d = 1800$ kg/m^3, $E^* = 126$ GPa for Be on Be, $E^* = 160$ GPa for Be on W, $v = 1$ m/s and $D = 1.2 \times 10^{-5}$ m^2/s as an upper-bound estimation for Be at temperatures up to 1500 K [30], the ratio t_{Hertz}/t_0 lies below 5 % for all relevant dust radii. Contact cooling can therefore be neglected in the

simulations, while it can be assumed that the particles rapidly cool down to T_w once they are stuck to the wall since t_0 is at most a few tens of milliseconds, that is much smaller than the typical particle time of flight in the vessel.

2.5. Simulation parameters and vessel geometry

Although numerical modelling of metallic melt layer dynamics under ITER-relevant conditions is available [5, 31, 32, 33], to our knowledge, no experimental validations currently exist regarding the size, speed and angle distributions of Be droplets. Experimental observations of Be plasma-facing component heating after VDEs in JET [34, 35] suggest a droplet size of the order of a few μm, but the extrapolation of these results to ITER is uncertain due to the upscaling of plasma energy and machine size. More detailed experiments on W droplets in plasma guns report typical sizes of several tens of μm [36, 37, 38, 39, 40] and most probable ejection speeds of a few m/s, which are expected to increase by a factor $\lesssim 3$ in the case of Be due to the main scaling with mass density [5, 31, 37, 38, 40, 41]. Given those uncertainties, the choice is made here to scan a wide enough range of droplet characteristics so as to capture the influence of these parameters and draw generic conclusions on droplet cooling. More specifically, the initial droplet radius is varied between 1 μm and 500 μm by steps of 1 μm and the initial droplet speed between 1 m/s and 10 m/s by steps of 1 m/s. The direction of injection is chosen among 65 values that mesh the half-full solid angle such that the injection angle with respect to wall normal varies between 0 degrees and 80 degrees by steps of 10 degrees. The droplet injection position is set at the junction between the first wall panels 10 and 11, at the expected plasma contact point during a VDE [42].

In the simulations, the disrupting plasma is set with $n_e = 1.5 \times 10^{20}$ m^{-3}, $T_e = T_i = 5$ eV and $\tau_{\text{plasma}} = 50$ ms. The mitigating gas is assumed to be Ar or Ne and the presence of steam is included to simulate cases in which a water leak occurs during the disruption. The properties of the gas background, summarized in table 1, are varied with respect to a reference scenario consisting of pure Ar at room temperature and a pressure of 10 Pa. In the cases which include water vapour, its pressure is varied around 100 Pa, which is the value estimated from the expected leaking rate of damaged coolant pipes. The simulations are carried out in toroidally symmetric geometry with a Be main chamber wall and a W divertor. In the following sections, the simulated spatial distribution of the dust particles on the wall after the disruption is presented using a curvilinear coordinate s along the poloidal cross-section of the vessel, as detailed in figure 3.

	Ar	Ne	H_2O
Heat capacity ratio γ_g	1.67	1.67	1.33
Molecular mass m_g [kg]	6.68×10^{-26}	3.38×10^{-26}	2.99×10^{-26}
Pressure p_g [Pa]	10	10	$0 - 200$
Temperature T_g [K]	$300 - 3500$	$300 - 3500$	350
Mean free path λ_g [μm]	660	983	1230
Heat transfer coefficient h_g [W/(m^{2}K)]	4.41	6.24	17.6

Table 1: Gas properties for the species considered in the simulations. The values of λ_g and h_g are given at room temperature and a pressure of 10 Pa, without the correction for finite Knudsen numbers.
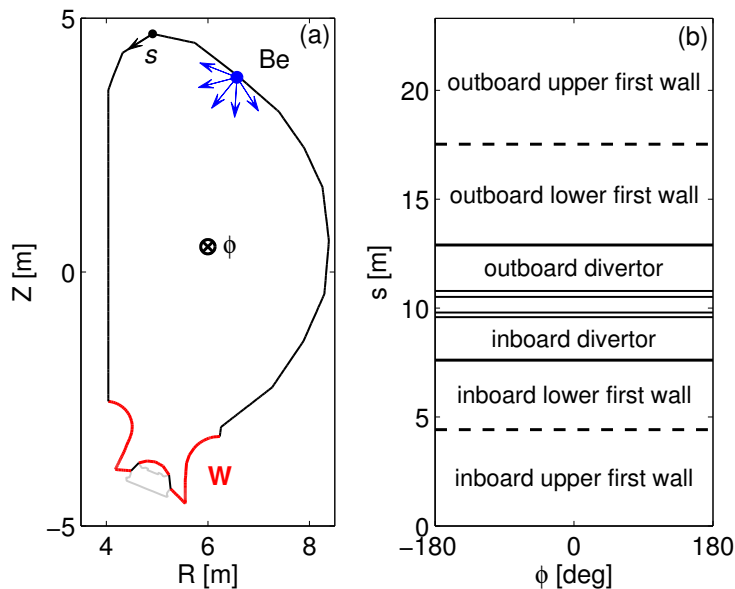

Figure 3: (*a*) Poloidal cross-section of the ITER plasma chamber as implemented in MIGRAINe. The gaps between the dome and the reflector plates are modelled as perfectly absorbing boundaries for dust particles. The droplet injection point is marked, and the origin and orientation of the poloidal wall coordinate s are indicated. ϕ denotes the toroidal angle, with $\phi = 0$ at the injection point. (*b*) Two-dimensional parametrization of the wall with its main regions indicated. The absorbing gaps lie within the double horizontal lines.

3. Results and discussion

With the parameters given above, the quenching plasma is hot and dense enough to rapidly bring all the droplets to a regime of strong vaporization, in which plasma heating is balanced by vaporization cooling, resulting in a steady value of the droplet temperature which is approximately 2000 K in the simulations reported here and depends weakly on the plasma parameters. As long as the plasma remains present, R_d decreases at a constant rate depending only on T_d. Here, $|dR_d/dt| \sim 0.2 \ \mu\text{m/ms}$, so that independently of their initial size, the droplets have their radius reduced by $\sim 10 \ \mu\text{m}$ after a 50 ms plasma stage; the ones below that size limit get entirely vaporized.

It is important to mention at this point that the charging and heating model [8] used to simulate the plasma stage relies on the orbital motion limited theory (OML) [43], whose validity requires R_d to be smaller than the Debye length and the gyro-radius of the plasma species. These assumptions are not satisfied in the case considered here, since the electron Debye length and gyro-radius both are of the order of 1 μm, and the ion gyro-radius – assuming a deuterium plasma – is approximately 60 μm. There currently is no complete theory describing the charging and heating of metal particles in all fusion-relevant regimes, and a self-consistent treatment of both processes is particularly problematic since existing models for probes in magnetized plasmas yield expressions for the total currents rather than collection cross-sections (see e.g. [44] and references therein). In the case where only electrons are magnetized on the droplet scale, corresponding here to $R_d \leq 60 \ \mu\text{m}$, the electron current collected by the droplet is reduced compared to OML values [45], while ion collection is inhibited by absorption radius effects [46, 47, 48]. As a consequence, the total heat flux on the droplet is expected to decrease by a factor 2 at most. For $R_d \gg 60 \ \mu\text{m}$, the geometry of the problem is effectively planar, leading to estimates of the total heat flux $\sim 50 \ \%$ below the OML predictions [49]. A lower heat flux to the droplet delays the onset of the strong vaporization regime, which for the largest sizes (above 300 μm in radius) may not occur before the end of the 50 ms plasma stage. Therefore, the mass lost by the droplets would be lower than predicted here, but the temperature saturation at 2000 K and the subsequent evolution of the droplets during the gas stage would only be weakly affected.

3.1. Cooling regimes during the gas stage

As safety issues related to Be droplets mainly concern hydrogen production from hot Be in case of loss-of-coolant accidents, the time during which the droplets remain hot enough

to react is chosen as a figure of merit in the analysis of the cooling process. The indicative temperature threshold for Be reactivity varies in the available literature [1, 18, 19]; here, it is set at 800 K, noting that the results are not qualitatively affected by a change of its value by ± 100 K.

On a general note, cooling from thermal radiation and heat exchange with the ambient gas is more efficient for smaller particles due to their higher surface-volume ratio, so that the time t_{800} required for a droplet to reach 800 K is expected to be essentially proportional to R_{d}, with slight corrections stemming from the temperature dependence of material properties. However, since a sticking or splashing collision is followed by an instantaneous drop of the particle temperature to T_{w}, t_{800} is bounded by the particle time of flight inside the vessel. This leads to the emergence of two limiting regimes: (i) in the case of very small droplets, t_{800} is entirely determined by the gas background and the droplet size via equation (1); (ii) conversely, in the case of very large droplets, cooling processes are too slow to allow their solidification before they hit the wall and t_{800} is equal to the droplet time of flight, which depends only on geometrical parameters – the initial droplet velocity and the shape of the vessel.

The critical values of R_{d} corresponding to these two cooling regimes can be visualized by examining the statistical distribution of t_{800} within sub-populations of a given initial size, as shown in figure 4. After the first size threshold, variations in the initial droplet velocity widen the statistical distribution of t_{800} and cause it to depart from its purely gas-dependent behaviour. The slope of the curve decreases as more particles end up sticking before having cooled down to 800 K, until a second size threshold is reached, above which all the particles undergo their first collision while in liquid state. The boundaries of the intermediate size range are determined by the gas mixture in the vessel. In particular, the presence of water vapour can significantly increase the heat transfer coefficient and shift the critical radii to higher values, as demonstrated in figure 5.

3.2. Spatial distribution of adhered grains and splashes

Be particles adhered on plasma-facing components contribute to the global dust inventory of ITER. Those residing on hot surfaces are of particular concern as they are susceptible to become chemically active during accidents. Moreover, depending on their position, loosely-attached grains might get remobilized, vaporize into impurities in the scrape-off layer, or migrate towards more hazardous regions of the vessel. It is therefore necessary to identify the preferred locations of adhesion sites. In the following
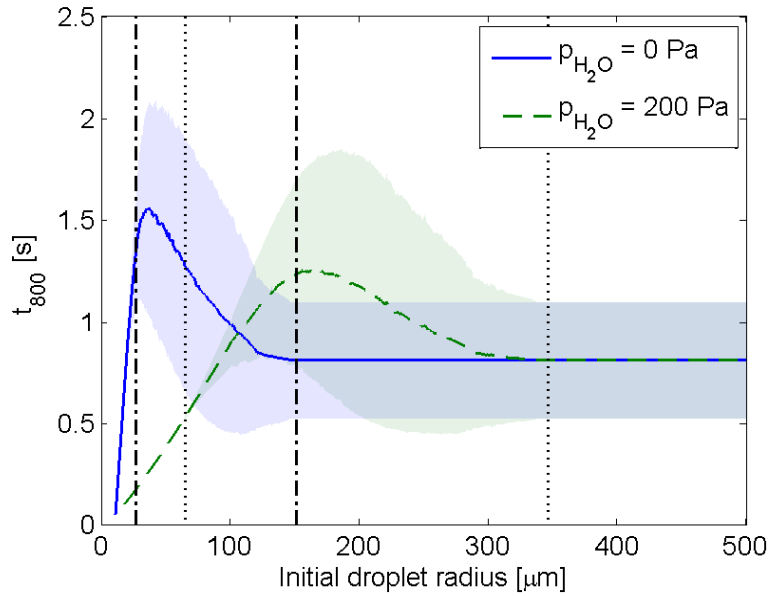
Figure 4: Plot of t_{800} as a function of the initial droplet radius for room-temperature Ar at 10 Pa, with and without water vapour. The solid lines show the average over the droplets with given initial size and the shaded areas indicate the standard deviation. Transitions between cooling regimes are highlighted by the pairs of vertical lines.
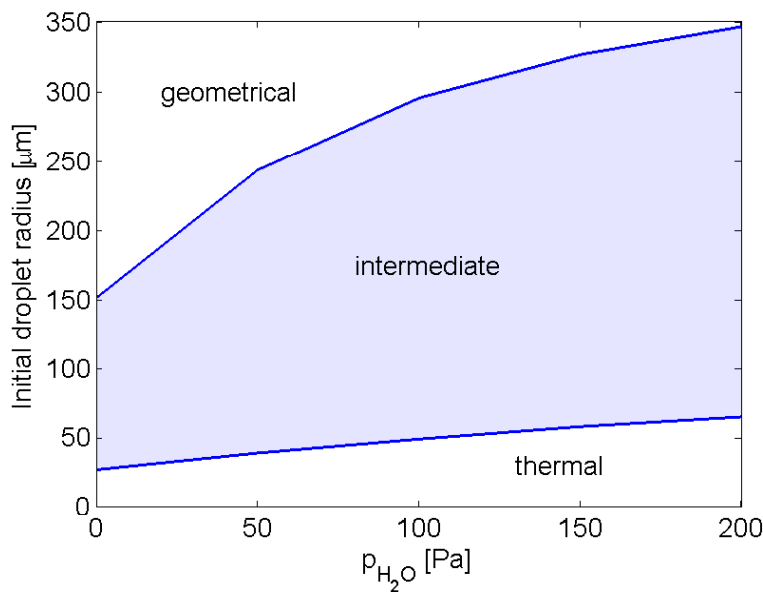

Figure 5: Delimitation of the three cooling regimes as a function of the initial droplet radius and the pressure p_{H_2O} of water vapour for room-temperature Ar at 10 Pa.

analysis, the distinction is made between the particles that solidified before hitting the wall, conserving an approximatively spherical shape, and those that hit the wall while in liquid state. Solidified grains are potentially subject to remobilization [22], while splashes left by droplet impacts are likely only affected by material migration processes at the atomic scale.

The spatial distribution of re-solidified dust in the reference scenario is shown in figure 7(a). It can be seen that the particles are potentially able to migrate toroidally over the whole machine, but that most of them are found in the bottom part of the vessel, preferably on the outboard side. The few grains residing above the midplane are located across the droplet injection point in the poloidal cross-section and are bounded toroidally. The average initial radius, shown in figure 7(b), indicates that smaller particles – typically below 50 μm in radius – have a significant poloidal spread, whereas larger particles tend to accumulate in the divertor legs and below the dome. This can be explained by the size dependence of the sticking velocity, which implies that small particles likely undergo few collisions with the wall before they stick. On the contrary, large particles can bounce multiple times and remain in motion long enough for gravity to drive them to the lowest parts of the machine. The asymmetry between the inboard and outboard sides is a direct consequence of the centrifugal effects in toroidal geometry. The importance of collisions on particle transport is illustrated by the typical examples of droplet trajectories shown in figure 8.

Figures 7(c) and (d) quantify the influence of the initial droplet velocity: slow (below 5 m/s) and normal (below 30°) injections result in a rather weak spread of the adhesion sites in both directions, whereas fast and tangential injections result in a significantly enhanced ability to migrate. This result is consistent with the fact that faster particles are allowed a larger number of collisions with the wall before they stick, and that those injected tangentially have a larger toroidal velocity component. Despite the upper limitation set to 10 m/s in the simulations, the results can readily be extrapolated to higher injection speeds.

Improving the droplet cooling efficiency by including water vapour in the background gas does not qualitatively affect the spatial distribution of the adhesion sites. As discussed in section 3.1, the effect mainly consists in allowing the solidification of larger droplets, which can then collide multiple times with the wall owing to their small sticking velocity. These particles tend to remain in motion for durations up to several seconds, leading to a stronger dust accumulation in the divertor legs and below the dome, as detailed in figure 9.
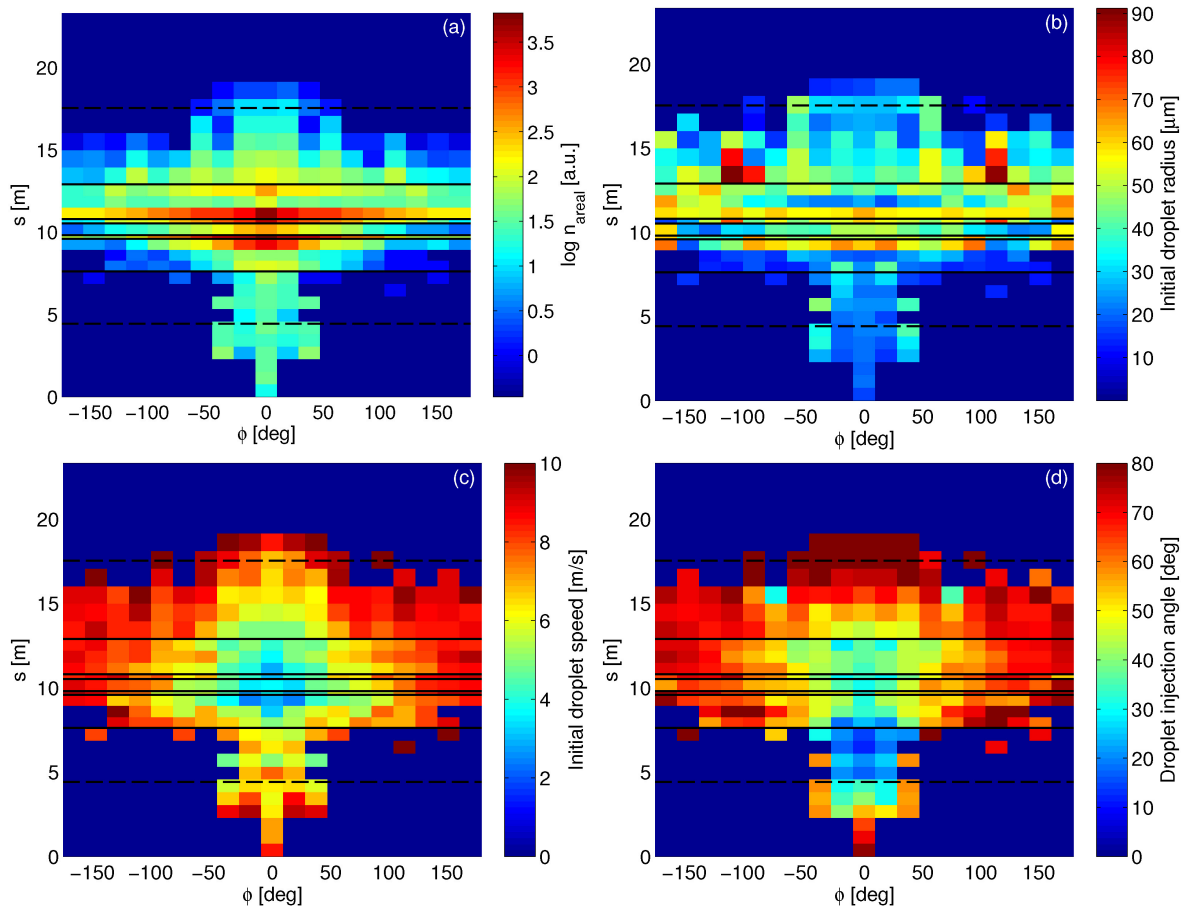
Figure 7: Spatial distribution of the solidified dust grains on the vessel wall in the reference scenario (room-temperature Ar at 10 Pa). (*a*) Areal dust particle density, (*b*) average initial droplet radius, (*c*) average injection speed, (*d*) average injection angle with respect to the local normal.

The spatial distribution of liquid splashes is directly related to the ballistic trajectories starting from the droplet source and is therefore unaffected by the composition of the gas background. The detailed distribution, plotted in figure 11 as a function of the initial droplet velocity, suggests the same qualitative conclusions as figures 7(*c*) and (*d*). The most noticeable difference lies in the impossibility of long-distance migration via multiple bouncing, so that even the droplets injected tangentially at 10 m/s cannot travel further than $\sim 90°$ toroidally away from their initial position.

3.3. Influence of the mitigating gas properties

In light of the analysis presented in section 3.1, it can be expected that the properties of the mitigating gas mostly affect the small droplets belonging to the 'thermal' regime.
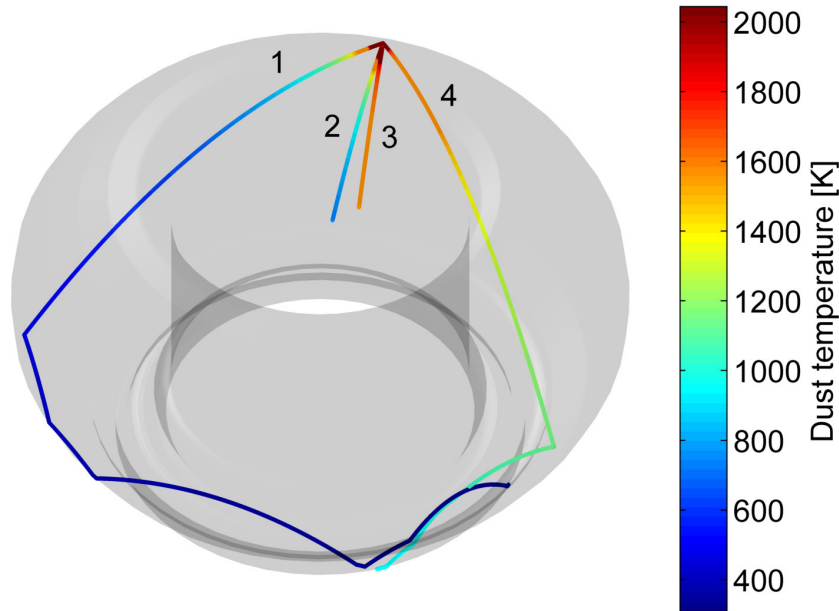
Figure 8: Examples of simulated 3D droplet trajectories in ITER for various initial conditions. Trajectory #1: tangential injection with initial radius 15 μm, collisions between the particle and the wall are affected by surface roughness, occasionally resulting in an increase of (apparent) normal velocity. Trajectory #2: normal injection with initial radius 15 μm, the re-solidified particle sticks upon its first collision. Trajectory #3: normal injection with initial radius 100 μm, the droplet is still liquid when it hits the wall. Trajectory #4: tangential injection with initial radius 50 μm, the re-solidified particle loses a significant fraction of its kinetic energy every time it collides with the wall.

Considering a single gas species at a given temperature and pressure, the characteristic cooling time due to conductive heat transfer deduced from equation (1) is expected to scale as the square root of the gas atomic mass, implying that the variations in cooling time due to the choice of Ar or Ne should remain within 30 % in the 'thermal' regime and progressively vanish towards the 'geometrical' regime. In fact, MIGRAINe simulations show that the variation of t_{800} is at most 10 % in cases without water vapour, and quickly becomes negligible when water vapour is added to the gas mixture. These effects are imputable to the importance of radiation cooling – which dominates for $T_\mathrm{d} > (h_\mathrm{g}/\varepsilon_\mathrm{d}\sigma)^{1/3} \sim 800$ K, taking $\varepsilon_\mathrm{d} = 0.2$ as the representative thermal emissivity of Be – and the fact that water vapour with a pressure of several tens of Pa provides the dominant contribution to the thermal properties of the gas mixture, as evident from table 1.
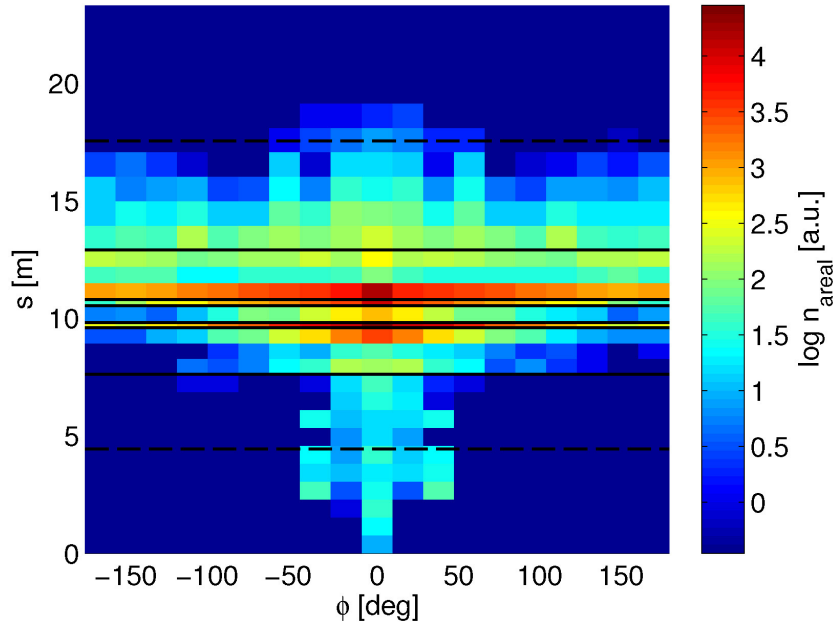
Figure 9: Spatial distribution of the solidified dust particle areal density for room-temperature Ar at 10 Pa with 200 Pa of water vapour.
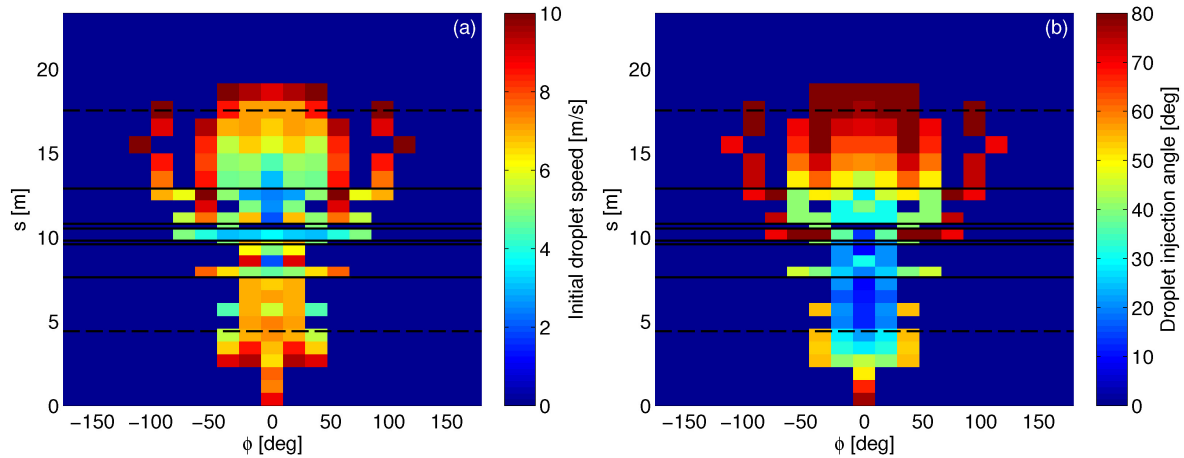

Figure 11: Spatial distribution of the droplet splashes as a function of (*a*) the average injection speed and (*b*) the average injection angle with respect to the local normal.

The impact of the gas temperature T_g is more difficult to assess directly from the model equations as a hot enough mitigating gas might start to heat the droplets instead of cooling them, resulting in inhibited migration and stronger chemical reactivity of the small droplets. The effect of elevated Ar temperatures on t_{800} is presented in figure 12, which shows that the predicted cooling time significantly departs from the reference scenario for droplets with an initial radius below ~ 30 μm. Above a certain threshold of about 2000 K, the results cease to depend on the gas temperature as the 'thermal'
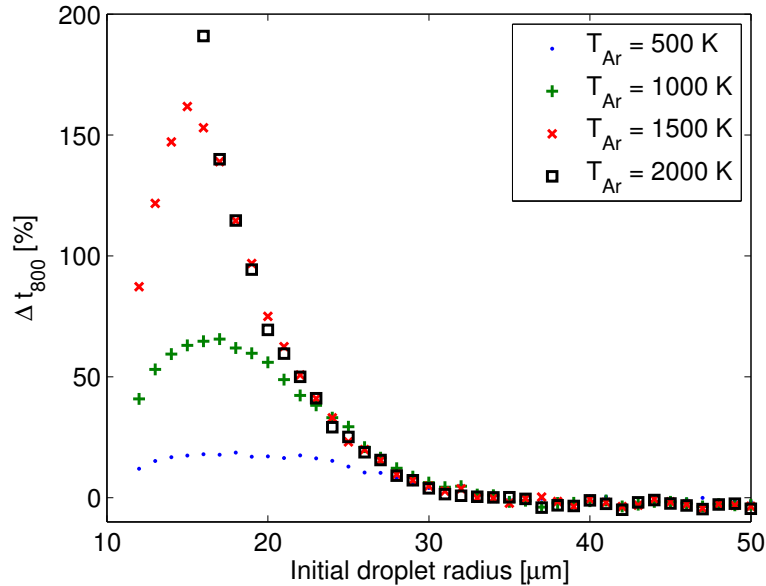
Figure 12: Relative variation of the average value of t_{800} with respect to the reference scenario for Ar at 10 Pa and various temperatures. In the 2000 K case, t_{800} increases by a factor up to 8 for the smallest droplets (not plotted for better readability).

cooling regime becomes irrelevant and t_{800} becomes equal to the particle time of flight. It can also be seen that for initial droplet radii above 30 μm, t_{800} decreases with respect to the reference scenario, which is due to the higher sticking velocity of hotter dust grains.

3.4. Effect of nano-scale wall roughness

In addition to the geometric effects of micrometre-scale asperities, surface roughness at the nanometre scale is expected to affect dust-wall collisions by reducing adhesive forces, and hence the sticking velocity. Nanometric roughness was implemented in simulations as in [9], by randomizing the sticking velocity at every impact between 0 and its value for smooths surfaces. As a result, solid grains are allowed to undergo a larger number of collisions with the wall before they stick and their time of flight (including bouncing) is increased. Figure 13 shows that this increase mostly affects the grains initially smaller than 50 μm – reaching up to 40 % for the smallest sizes – and does not strongly depend on the properties of the gas background. In contrast to micrometric roughness, for which the grain size enters explicitly in the model, the size dependence observed in the figure is linked the physics of energy dissipation upon dust-wall impacts. Whereas adhesion is a significant dissipative process for small particles, large particles mainly lose their
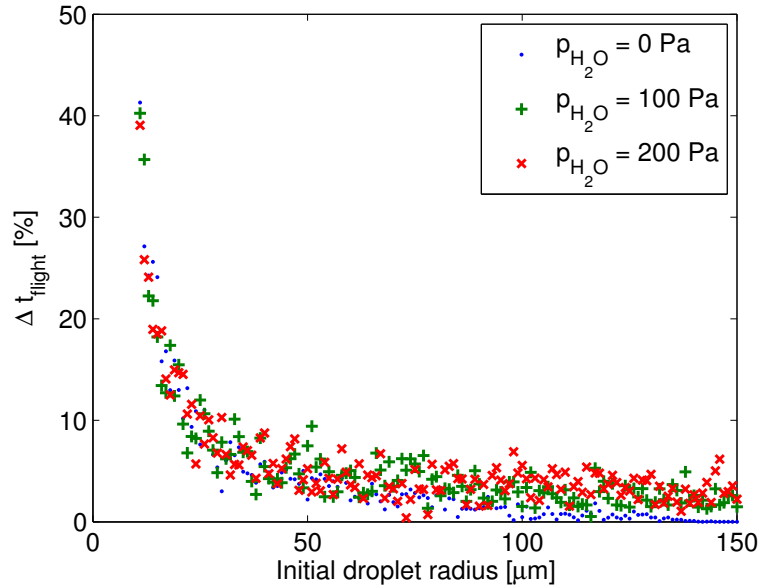
Figure 13: Relative increase of the average particle time of flight due to nano-scale wall roughness for room-temperature Ar at 10 Pa with various amounts of water vapour.

kinetic energy via plastic deformations, which are unaffected by surface roughness.

4. Conclusions

MIGRAINe simulations of the dynamics of molten Be particles created by VDEs in ITER underline the importance of the characteristic droplet size as the main parameter of interest with respect to safety issues associated by the chemical reactivity of hot Be. Three major cooling regimes have been derived, which impact not only the temperature evolution of the droplets, but also their ability to migrate in the vacuum vessel by bouncing on the plasma-facing components. Whereas droplets below 50 μm in radius are expected to be deposited rather uniformly in the divertor chamber and the lower outboard first wall after their solidification, larger solid grains can undergo multiple collisions before being immobilized, leading them to accumulate in the divertor legs and under the dome. Droplets with an initial radius above 150 μm are typically too large to solidify before they hit the wall, thus they were assumed to be immobilized at their first collision and form a molten splash upon impact. However, it is noteworthy that bouncing impacts of liquid droplets on solid surfaces are in principle possible in some regimes [50].

The influence of the initial droplet velocity on the location of Be dust deposition

sites has been studied. The results indicate that initial speeds below 5 m/s and normal injection angles below 30° tend to confine the particles within a quarter of the torus. On the contrary, droplets ejected tangentially with high speeds can cover the whole range of toroidal angles.

The composition and temperature of the mitigating gas are shown to affect mainly the temperature evolution of the particles smaller than 30 μm in radius. While the choice of Ar or Ne has little impact on the results, gas temperatures above 1000 K can increase the characteristic cooling time of small droplets from hundreds of milliseconds to a few seconds. The presence of water vapour in the plasma chamber in case of plasma-facing component failure is shown to significantly enhance droplet cooling, which, on the one hand, allows the solidification of particles up to 300 μm in radius, and on the other hand limits the chemical reactivity of Be.

Acknowledgments

References

[1] Rosanvallon S, Grisolia C, Andrew P *et al.* 2009 *J. Nucl. Mater.* **390–391** 57
[2] Shimada M, Pitts R A, Ciattaglia S *et al.* 2013 *J. Nucl. Mater.* **438** S996
[3] Hassanein A 2002 *Fusion Eng. Des.* **60** 527
[4] Garkusha I E, Makhlaj V A, Cheboratev V V *et al.* 2009 *J. Nucl. Mater.* **390–391** 814
[5] Bazylev B, Landman I, Loarte A *et al.* 2009 *Phys. Scr.* **T138** 014061
[6] Kupriyanov I B, Nikolaev G N, Kurbatova L A *et al.* 2015 *J. Nucl. Mater.* **463** 781
[7] Flanagan J C, Sertoli M, Bacharis M *et al.* 2015 *Plasma Phys. Control. Fusion* **57** 014037
[8] Vignitchouk L, Tolias P and Ratynskaia S 2014 *Plasma Phys. Control. Fusion* **56** 095005
[9] Ratynskaia S, Vignitchouk L, Tolias P *et al.* 2013 *Nucl. Fusion* **53** 123002
[10] Delzanno G L and Tang X Z 2014 *Phys. Rev. Lett.* **113** 035002
[11] Bohren C F and Huffman D R 1983 *Absorption and Scattering of Light by Small Particles* (Weinheim: Wiley Interscience)
[12] Chi T C 1979 *J. Phys. Chem. Ref. Data* **8** 439
[13] Devienne F M 1965 Low density heat transfer *Advances in Heat Transfer* (New York: Academic Press) pp 271–356
[14] Eckstein W 2009 Reflection (Backscattering) Tech. Rep. IPP 17/12 Max Planck Institute for Plasma Physics

[15] Sharpe J P, Petti D A and Bartels H W 2002 *Fusion Eng. Des.* **63–64** 153

[16] Tillack M S, Humrickhouse P W, Malang S and Rowcliffe A F 2015 *Fusion Eng. Des.* **91** 52

[17] McCarthy K A, Petti D A, Carmack W J and Smolik G R 1998 *Fusion Eng. Des.* **42** 45

[18] Anderl R A, Pawelko R J, Smolik G R *et al.* 2002 *J. Nucl. Mater.* **307–311** 1375

[19] Filatov V 2002 *Plasma Devices Oper.* **10** 215

[20] Thornton C and Ning Z 1998 *Powder Technol.* **99** 154

[21] Shalpegin A, Brochard F, Ratynskaia S *et al.* 2015 *Nucl. Fusion* **55** 112001

[22] Tolias P, Ratynskaia S, De Angeli M *et al.* 2016 *Plasma Phys. Control. Fusion* **58** 025009

[23] Uchic M D, Dimiduk D M, Florando J N and Nix W D 2004 *Science* **305** 986

[24] Schneider A S, Kaufmann D, Clark B G *et al.* 2009 *Phys. Rev. Lett.* **103** 105501

[25] ITER Vacuum Handbook

[26] Holm R 1967 *Electric Contacts – Theory and Applications* (Berlin: Springer)

[27] Yovanovich M M 2005 *IEEE T. Compon. Pack. T.* **28** 182

[28] Ratynskaia S, Tolias P, Bykov I *et al.* 2016 *Nucl. Fusion* Submitted

[29] Johnson K L 1987 *Contact Mechanics* (Cambridge: Cambridge University Press)

[30] Dalle Donne M *et al.* 1991 KfK Contribution to the Development of DEMO-Relevant Test Blankets for NET/ITER Tech. Rep. KfK 4929 Karlsruhe Institute of Technology

[31] Bazylev B, Janeschitz G, Landman I *et al.* 2009 *Fusion Eng. Des.* **84** 441

[32] Bazylev B, Igitkhanov Y, Landman I *et al.* 2011 *J. Nucl. Mater.* **417** 655

[33] Martynenko Y V 2014 *Problems of Atomic Science and Technology. Ser. Thermonuclear Fusion* **37** 53

[34] Lehnen M, Arnoux G, Hartmann N *et al.* 2013 *J. Nucl. Mater.* **438** S102

[35] Baron-Wiechec A, Fortuna-Zaleśna E, Grzonka J *et al.* 2015 *Nucl. Fusion* **55** 113033

[36] Garkusha I E, Arkhipov N I, Klimov N S *et al.* 2009 *Phys. Scr.* **T138** 014054

[37] Klimov N, Podkovyrov V, Zhitlukhin A *et al.* 2011 *J. Nucl. Mater.* **415** S59

[38] Arzhannikov A V, Bataev V A, Bataev I A *et al.* 2013 *J. Nucl. Mater.* **438** S677

[39] Makhlaj V A Garkusha I E, Aksenov N N *et al.* 2013 *J. Nucl. Mater.* **438** S233

[40] Makhlaj V A Garkusha I E, Aksenov N N *et al.* 2014 *Phys. Scr.* **T159** 014024

[41] Shoshin A A, Arzhannikov A V, Burdakov A V *et al.* 2011 *Fusion Sci. Technol.* **59** 57

[42] Mitteau R, Sugihara M, Raffray R *et al.* 2011 *Phys. Scr.* **T145** 014081

[43] Mott-Smith H and Langmuir I 1926 *Phys. Rev.* **28** 727

[44] Demidov V, Ratynskaia S and Rypdal K 2002 *Rev. Sci. Instrum.* **73** 3409

[45] Sanmartin J R 1970 *Phys. Fluids* **13** 103

[46] Allen J E, Boyd R L F and Reynolds P 1957 *Proc. Phys. Soc.* **70** 297

[47] Bernstein I B and Rabinowitz I N 1959 *Phys. Fluids* **2** 112

[48] Laframboise J G 1959 Theory of spherical and cylindrical Langmuir probes in a collisionless, Maxwellian plasma at rest Tech. Rep. UTIAS 100 University of Toronto Institute for Aerospace Studies

[49] Stangeby P C 1989 The interpretation of plasma probes for fusion experiments *Plasma Diagnostics: Surface Analysis and Interactions* (San Diego: Academic Press) pp 157–209

[50] Rein M 1993 *Fluid Dyn. Res.* **12** 61